Nuclear Instruments and Methods in Physics Research A 828 (2016) 145–155

Contents lists available at ScienceDirect

Nuclear Instruments and Methods in Physics Research A

journal homepage: www.elsevier.com/locate/nima

Estimation method of planetary fast neutron flux by a Ge gamma-ray spectrometer

M. Hareyama [a,*], Y. Fujibayashi [b], Y. Yamashita [e], Y. Karouji [c], H. Nagaoka [b], S. Kobayashi [d], R.C. Reedy [e], O. Gasnault [f], O. Forni [f], C. d'Uston [f], K.J. Kim [g], N. Hasebe [b]

[a] Department of Physiology, St. Marianna University School of Medicine, 2-16-1 Sugao, Miyamae-ku, Kawasaki, Kanagawa 216-8511, Japan
[b] Research Institute for Science and Engineering, Waseda University, 3-4-1 Okubo, Shinjuku-ku, Tokyo 169-8555, Japan
[c] Institute of Space and Astronautical Science, Japan Aerospace Exploration Agency, 3-1-1 Yoshinodai, Chuo-ku, Sagamihara, Kanagawa 252-5201, Japan
[d] National Institute of Radiological Sciences, 4-9-1 Anagawa, Inage-ku, Chiba 263-8555, Japan
[e] Planetary Science Institute, Tucson, AZ 85719, USA
[f] Institut de Recherché en Astrophysique et Plane Planétotologie, Université de Toulouse/CNRS, 9 Avenue Colonel Roche, Toulouse F-31400, France
[g] Korea Institute of Geosciences and Mineral Resources, 92 Gwahang-no, Yuseong-gu, Daejeon 305-350, Republic of Korea

ARTICLE INFO

Article history:
Received 11 November 2015
Received in revised form
6 May 2016
Accepted 10 May 2016
Available online 12 May 2016

Keywords:
Fast neutron
HPGe detector
Gamma ray spectrometer
Moon
Kaguya
SELENE

ABSTRACT

An intensity map of lunar fast neutrons (LFNs) and their temporal variation has been estimated by fitting "sawtooth" peaks in the energy spectra of lunar gamma rays observed by the Kaguya (SELENE) Gamma Ray Spectrometer (GRS) consisting of a high-purity germanium (HPGe) detector with a BGO scintillator. While an ordinary peak in the spectrum is produced by only gamma ray lines, the sawtooth peak is produced by gamma ray lines and recoil nuclei in the detector by Ge(n, n′γ) reaction. We develop a model for the shape of the sawtooth peak and apply it to fit sawtooth peaks together with ordinary peaks in actual observed spectra on the Moon. The temporal variation of LFNs is synchronous with that of galactic cosmic rays (GCRs), and the global distribution of fast neutrons on the lunar surface agrees well with the past observation reported by the Neutron Spectrometer aboard Lunar Prospector. Based on these results, a new method is established to estimate the flux of fast neutrons by fitting sawtooth peaks on the gamma ray spectrum observed by the HPGe detector.

1. Introduction

Gamma ray spectrometers (GRSs) have been employed by lunar and planetary explorers such as Lunar Prospector [1], Mars Odyssey [2], Kaguya (SELENE) [3] and MESSENGER [4] to determine the chemical compositions of lunar and planetary surfaces. The gamma rays emitted from a planet are generated as a result of the collision of neutron with nucleus in both the atmosphere and the regolith of the planet. These gamma rays observed by GRS on planetary orbit consist of gamma ray lines by nuclear interaction of neutron with the planetary materials (e.g., neutron capture and nonelastic scattering depend on neutron energy) and continuum components by some electromagnetic processes during traveling there. In addition, gamma ray lines of natural radioisotopes as potassium, thorium and uranium in the planet emitted by radioactive decay are observed. As a result, the spectrum observed by GRS on planetary orbit has many gamma ray peaks reflecting to the chemical composition of the planet. While, since neutrons colliding with the planetary materials are generated by collision of galactic cosmic ray (GCR) with nucleus in the atmosphere and the regolith, neutron fluxes also reflect the chemical composition of the planet. Actually, the Lunar Exploration Neutron Detector onboard Lunar Reconnaissance Orbiter made the hydrogen map on the lunar surface [5,6], and the neutron spectrometer onboard Lunar Prospector presented the average atomic mass map of the lunar surface [7]. Therefore, neutron and gamma ray spectroscopy can be used as a tool to better understand and constrain the concentration of major, minor, and trace elements in the atmosphere, surface and near-subsurface of planetary bodies in the Solar System.

Planetary neutron flux generated by GCR varies with regional variation of the chemical abundance, and it is moderated by collision with the planetary materials during passing through there. Also, the neutron flux is in proportion to GCR flux, which is in inverse proportion to the solar activity (e.g. [8,9]). In case of an airless body such as the Moon, both energy spectra of neutrons depend only on the chemical composition of the regolith and GCR flux. For the Moon, collision mean free path of GCR proton in the regolith is about 100 g/cm^2 and about 1 m in depth from the lunar surface. Neutrons produced by GCR interactions at 1 m in depth

---

[*] Corresponding author.
E-mail address: m-hareyama@marianna-u.ac.jp (M. Hareyama).

http://dx.doi.org/10.1016/j.nima.2016.05.045
0168-9002/© 2016 Elsevier B.V. All rights reserved.

leak from the lunar surface while being modulated through neutron-nuclei interactions with the regolith as modulating materials depending on water (H) content. Gamma ray lines are produced during this processes. Absorption length of gamma rays in the lunar subsurface is about several 10 g/cm^2 and several 10 cm in depth depending on water (H) content. Thus, gamma rays induced by the planetary neutrons have to be corrected by those intensity in order to estimate concentration of element on the planet [1].

In this point of view, gamma ray spectroscopy measurement on the planetary orbit should be conducted simultaneously using both a neutron and a gamma ray spectrometer. However, the neutron detector may break down, or a satellite may not carry a detector. In fact, no neutron spectrometer was onboard Kaguya. In such cases, we must estimate neutron flux using other means. One possibility is to use gamma ray lines emitted from detector materials themselves by interactions with neutrons. For instance, GRS on Mars Odyssey (MOGRS) having high-purity germanium (HPGe) crystal detected gamma ray lines of Ge emitted inside the HPGe detector by capturing thermal neutrons as Ge(n,γ) and inelastic scattering of fast neutrons as Ge(n, n′γ) [10]. For neutron capture, the peak shape is the same shape as ordinary gamma ray peaks because gamma rays are emitted only. However, for nonelastic scattering, the shape becomes triangular with a high-energy tail known as a “sawtooth peak”. A sawtooth peak is produced when the energy from the de-excitation of an excited level of Ge is summed with the recoil energy of a Ge nucleus introduced by interactions of fast neutrons in the detector [11]. That is, the sawtooth peak has a high-energy tail that depends on recoil energy distribution related to incident neutron energy. In case of Kaguya GRS, because the incident neutrons making the sawtooth peaks are originated by the interaction of GCRs with the lunar regolith, it may be possible to estimate lunar fast neutron flux by analyzing the peaks.

Many authors have studied the sawtooth peak in an HPGe detector on the Earth or in underground environments [12–18]. Especially, Siiskonen and Toivonen modeled the function of sawtooth peak and reported the neutron evaporation temperature based on the analysis of environmental monitoring gamma spectra [17]. For planetary and interplanetary environments other than the Earth, the sawtooth peaks were identified simply as background peaks in gamma ray spectra, but not analyzed themselves [10,19].

In this paper, we model a function of the sawtooth peak to fit it in the actual lunar gamma ray spectrum and estimate the relative flux of lunar fast neutrons (LFNs) observed by GRS on Kaguya (SELENE). Kaguya (SELENE) is a Japanese large-scale lunar explorer carrying 14 scientific instruments to determine the origin and evolution of the Moon [20]. One of these instruments is the Kaguya Gamma Ray Spectrometer (KGRS) that helps clarify the elemental distribution of major and trace elements on the lunar surface [3]. KGRS has an HPGe detector for gamma ray detection and a BGO scintillator for anti-coincidence. First, we derive a model function of the sawtooth peak taking into account the energy spectrum of LFN, cross sections of inelastic scattering, and the response function for KGRS. The model is applied in peak fitting to estimate counting rates of LFN from lunar gamma ray spectra. Finally, the results are used to develop a temporal variation and a lunar global map of LFN.

2. Model of peak functions

2.1. Peak function for an ordinary peak

In general, when gamma rays are detected by a GRS, a peak function of $P(E)$ is defined at an energy of E;

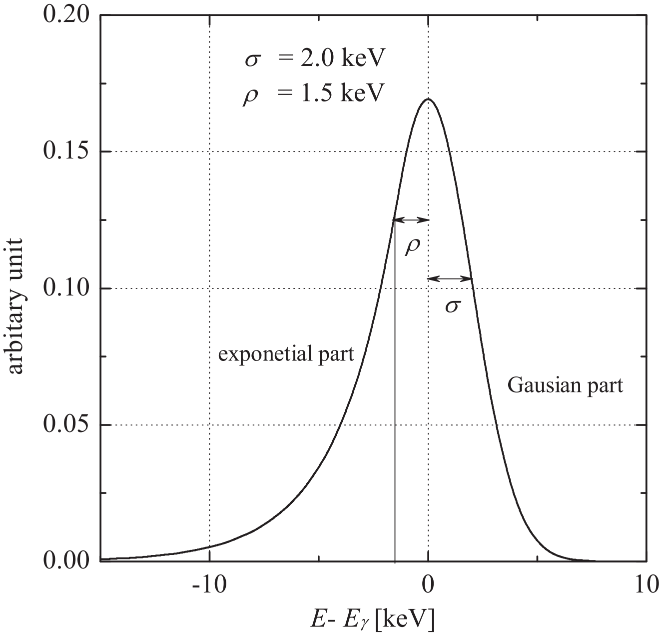

Fig. 1. Shape of the ordinary peak function for gamma ray lines. The peak function consists of a Gaussian part above the energy $E_\gamma - \rho$ and an exponential part below $E_\gamma - \rho$ for radiation damage. Here, σ is energy resolution, and ρ is damage energy expressing the degree of radiation damage of an HPGe detector.

$$P(E) = \int_0^\infty S(\varepsilon)\eta(E;\, \varepsilon)d\varepsilon, \tag{1}$$

where $S(\varepsilon)$ is a source function of gamma rays as incident energy ε, and $\eta(E;\, \varepsilon)$ is a response function of the detector.

Here, we consider gamma ray lines with energy E_γ emitted from a nuclide. Since the source function $S(\varepsilon)$ is expressed by δ function $\delta(\varepsilon - E_\gamma)$, the peak function becomes

$$P(E) = \int_0^\infty A\delta(\varepsilon - E_\gamma)\eta(E;\, \varepsilon)d\varepsilon = A\eta(E;\, E_\gamma), \tag{2}$$

where A is a source flux. This means that a peak shape made by gamma ray lines corresponds to a response function of the detector.

Since KGRS detected gamma rays using an HPGe detector in the same way as MOGRS, the following formulas used by MOGRS [10] are adopted for the peak function for gamma ray lines of energy E_γ (hereafter, the ordinary peak), which has Gaussian function with exponentially low energy tail due to radiation damage (see Fig. 1),

$$P(E) = \begin{cases} \dfrac{A}{\kappa}\dfrac{1}{\sqrt{2\pi}\sigma}\exp\left(\dfrac{\rho^2}{2\sigma^2}\right)\exp\left(\dfrac{(E - E_\gamma)\rho}{\sigma^2}\right) & (\text{if } E < E_\gamma - \rho) \\ \dfrac{A}{\kappa}\dfrac{1}{\sqrt{2\pi}\sigma}\exp\left(-\dfrac{(E - E_\gamma)^2}{2\sigma^2}\right) & (\text{if } E \ge E_\gamma - \rho), \end{cases} \tag{3}$$

$$\kappa = \frac{1}{\sqrt{2\pi}}\frac{\sigma}{\rho}\exp\left(-\frac{\rho^2}{2\sigma^2}\right) + \frac{1}{\sqrt{2\pi}}\int_{-\rho/\sigma}^{\infty}\exp\left(-\frac{y^2}{2}\right)dy. \tag{4}$$

Here A is the source intensity or a peak area, σ is the energy resolution recognized as the standard deviation of the Gaussian part, and ρ is energy expressing the degree of radiation damage of HPGe crystal [21] (hereafter, damage energy) (Fig. 1). As radiation damage increases, ρ decreases. κ is a normalization factor.

2.2. Peak function for a sawtooth peak

The high-energy tail of sawtooth peak is made by deposit energies caused through ionization by recoil Ge associated with Ge(n, n′γ) reaction in the Ge detector [11]. In other words, as the incident energy of projectile neutrons increases, the ionization energy of recoil Ge nuclei becomes larger and the tail becomes longer.

When the function of the long tail made by ionization energy of recoil Ge is assumed as a simple exponential decrease with a factor of $1/\langle T_{\mathrm{Ge}}\rangle$. This assumption has been used by Siiskonen and Toivonen [17]. The source function of the sawtooth peak becomes

$$S(\varepsilon) = \begin{cases} 0 & (\text{if } \varepsilon < E_\gamma) \\ \dfrac{A}{\langle T_{\mathrm{Ge}}\rangle} \exp\left(-\dfrac{\varepsilon - E_\gamma}{\langle T_{\mathrm{Ge}}\rangle}\right) & (\text{if } \varepsilon \geq E_\gamma). \end{cases} \tag{5}$$

In this work, $\langle T_{\mathrm{Ge}}\rangle$ denotes *effective* ionization energy.

As indicated in the previous section, the response function for KGRS is considered as the ordinary peak function for KGRS. The response functions become as follows using Eqs. (2) and (3);

$$\eta(E;\,\varepsilon) = \begin{cases} \dfrac{1}{\kappa}\dfrac{1}{\sqrt{2\pi}\sigma} \exp\left(\dfrac{\rho^2}{2\sigma^2}\right)\exp\left(\dfrac{(E-\varepsilon)\rho}{\sigma^2}\right) & (\text{if } E < \varepsilon - \rho) \\ \dfrac{1}{\kappa}\dfrac{1}{\sqrt{2\pi}\sigma} \exp\left(-\dfrac{(E-\varepsilon)^2}{2\sigma^2}\right) & (\text{if } E \geq \varepsilon - \rho). \end{cases} \tag{6}$$

Therefore, the peak function of sawtooth peak is given as follows (see details in Appendix C);

$$P(E) = \begin{cases} \dfrac{A\beta}{\kappa} \exp\left(\dfrac{\rho(E - E_\gamma + \rho)}{\sigma^2}\right) & (\text{if } E < E_\gamma - \rho) \\ \dfrac{A\beta}{\kappa} \exp\left(-\dfrac{E - E_\gamma + \rho}{\langle T_{\mathrm{Ge}}\rangle}\right)(\lambda\xi(E) + 1) & (\text{if } E \geq E_\gamma - \rho), \end{cases} \tag{7}$$

where

$$\xi(E) = \frac{1}{\sqrt{2\pi}} \int_{X(E)}^{X_{max}} \exp\left(-\frac{y^2}{2}\right) dy \tag{8}$$

$$\beta = \frac{1}{\sqrt{2\pi}} \frac{1}{X_{max}\langle T_{\mathrm{Ge}}\rangle} \exp\left(-\frac{\rho^2}{2\sigma^2}\right) \tag{9}$$

$$\lambda = \sqrt{2\pi} X_{max} \exp\left(\frac{X_{max}^2}{2}\right) \tag{10}$$

$$\kappa = \frac{1}{\sqrt{2\pi}} \frac{\sigma}{\rho} \exp\left(-\frac{\rho^2}{2\sigma^2}\right) + \frac{1}{\sqrt{2\pi}} \int_{-\rho/\sigma}^{\infty} \exp\left(-\frac{y^2}{2}\right) dy \tag{11}$$

$$X_{max} = \frac{\sigma^2/\langle T_{\mathrm{Ge}}\rangle + \rho}{\sigma} \tag{12}$$

$$X(E) = -\frac{E - E_\gamma - \sigma^2/\langle T_{\mathrm{Ge}}\rangle}{\sigma}. \tag{13}$$

This peak function, Eq. (7), is the same as that reported by Siiskonen and Toivonen [17], when parameter ρ becomes infinite; that is, the response function is Gaussian only (see also Appendix C).

The peak function defined by Eq. (7) has a peak top energy, E_p, satisfying the relation

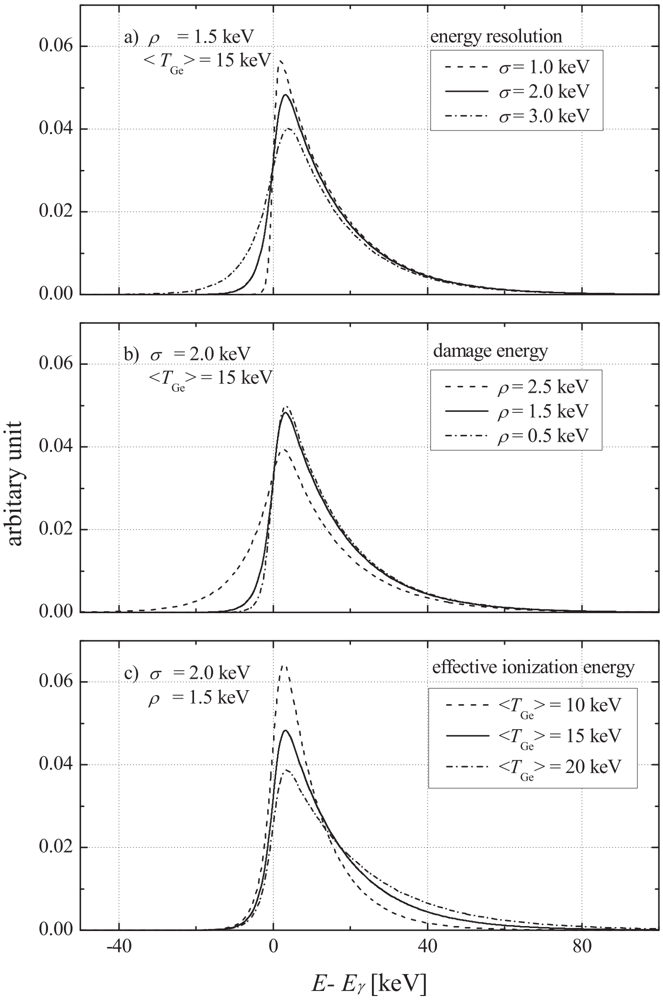

Fig. 2. Shape of sawtooth peak function. Each peak area is normalized to 1. (a) ρ and $\langle T_{\mathrm{Ge}}\rangle$ are fixed. (b) σ and $\langle T_{\mathrm{Ge}}\rangle$ are fixed. (c) σ and ρ are fixed.

$$E_p = E_\gamma + \sigma\left(\frac{\sigma}{\langle T_{\mathrm{Ge}}\rangle} + \sqrt{2\left[\ln\left(\frac{\langle T_{\mathrm{Ge}}\rangle}{\sqrt{2\pi}\sigma}\right) - \ln\left(\xi(E_p) + \frac{1}{\lambda}\right)\right]}\right). \tag{14}$$

Though E_p depends complicatedly on the parameters, it definitely shifts to higher energy from E_γ.

The shapes of the peak function defined by Eq. (7) for parameter sets, σ, ρ and $\langle T_{\mathrm{Ge}}\rangle$, are also shown in Fig. 2. The horizontal axis is the energy obtained by subtracting an emission energy of the gamma ray line E_γ; that is, 0 value corresponds to the emission energy of the gamma ray line. Comparing with the ordinary peak shown in Fig. 1, the position of peak top for any parameter sets shifts to the high energy side of several keV from an energy of gamma ray line. For change of $\langle T_{\mathrm{Ge}}\rangle$ (Fig. 2c), as $\langle T_{\mathrm{Ge}}\rangle$ becomes larger, length of the high-energy tail becomes longer. However, the change of the position of peak top and the width of the low-energy side is small. For the change of σ (Fig. 2a) and ρ (Fig. 2b) as comparing with Fig. 2c, the dependence of the change in the peak width of low energy side and the shift of peak top energy is large, but the change in the length of high energy tail is small dependence.

2.3. Effective ionization energy

The peak function defined by Eq. (7) has five parameters: A as peak area or counting rate, E_γ as gamma ray line energy, σ as energy resolution, ρ as damage energy, and $\langle T_{\mathrm{Ge}}\rangle$ as *effective* ionization energy. For these parameters, σ and ρ are determined experimentally by peak fitting of the ordinary peak, and E_γ is determined by assignment of a nuclide for each peak.

Here, we consider the *effective* ionization energy $\langle T_{\mathrm{Ge}} \rangle$. The sawtooth peak is made by $\mathrm{Ge(n, n'\gamma)}$ reaction of LFN in the HPGe detector. The energy spectrum of LFN, $dN(E_n)/dE_n$, has been reported using a simulation calculation by Yamashita et al. [22], and the cross sections of $\mathrm{Ge(n, n'\gamma)}$, $\sigma_n(E_n)$, have been reported as ENDF/B-VII.0 [23,24]. Using these data, we can estimate the relative frequency of LFN interaction for $\mathrm{Ge(n, n'\gamma)}$ in the detector expressed by $dI(En)/dEn$ as

$$\frac{dI(E_n)}{dE_n} \propto \frac{dN(E_n)}{dE_n}\sigma_n(E_n), \tag{15}$$

where E_n is the neutron energy.

The energy of the scattered neutron, E', and the recoil energy of Ge atom, E_R, after the reaction is given by Siiskonen and Toivonen [17] as

$$E' = \frac{M^2+1}{(M+1)^2}E_n + \frac{M}{M+1}Q + 2\cos\theta\sqrt{\frac{ME_n}{(M+1)^3}\left[Q + \frac{ME_n}{M+1}\right]}, \tag{16}$$

and

$$E_R = E_n - E' - E_x, \tag{17}$$

where M is the mass number of the target atom, θ is the scattering angle in the centre-of-mass coordinates, Q is the energy release in the reaction and E_x is the energy of the excited state ($Q = -E_x$). Since the scattering angle in the center of mass system can be treated as isotropic [17] the mean square of scattering energy becomes

$$\left\langle E'^2 \right\rangle = \left[\frac{M^2+1}{(M+1)^2}E_n + \frac{M}{M+1}Q\right]^2 + \frac{4}{3}\frac{ME_n}{(M+1)^3}\left[Q + \frac{ME_n}{M+1}\right], \tag{18}$$

and the mean recoil energy becomes also

$$\left\langle E_R \right\rangle = E_n - \sqrt{\left\langle E'^2 \right\rangle} - E_x \tag{19}$$

for an incident energy of neutron and an exited energy of a Ge atom.

The relationship between the recoil energy and the ionization energy E_i of Ge atom in HPGe detector has been presented by Ljungvall and Nyberg [18] as

$$E_i = aE_R^b, \tag{20}$$

where $a=0.21$ and $b=1.099$.

Thus, the frequencies of LFN interaction for exited energy are estimated as a function of the ionization energy as shown in Fig. 3. In case of 692 keV, the frequency in arbitrary unit is smaller than the others because cross section of this reaction is from a quarter to a few orders of magnitude less depending on incident energy of neutron than the others [23,24]. This work defines the *effective* ionization energy of $\langle T_{\mathrm{Ge}} \rangle$ as an average ionization energy weighted by the interaction frequency. The *effective* ionization energy may depend on energy spectrum of neutron. However, the energy spectra of LFN has approximately the same shape between the different lunar chemical compositions [22], lunar mare has richer in iron oxide and titanium oxide than the lunar highland. Therefore, the value of $\langle T_{\mathrm{Ge}} \rangle$ is considered as constant in this work. The numerical values are presented in Table 3 in Section 3.3.

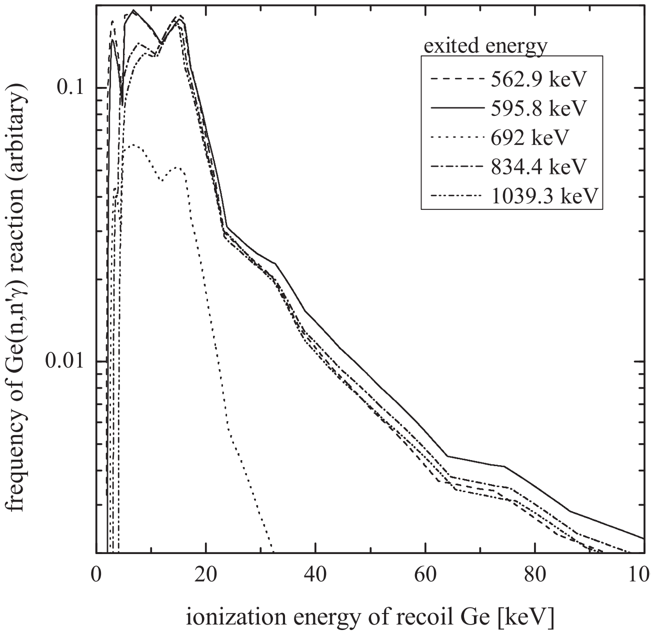

Fig. 3. Fluxes of $\mathrm{Ge(n, n'\gamma)}$ reaction in an HPGe detector as a function of ionization energy of the recoil Ge atom. The energy spectrum of incident neutron is adopted energy spectrum of lunar fast neutron [22]. The energies in the legend are excited energies for each reaction (See Table 3).

3. Observation and analysis

3.1. Observation

KGRS observed gamma rays emitted from the lunar surface between December 2007 and May 2009. This observation period is divided into three periods, due to changes of nominal flight height and applied voltage. Period I includes 32.90 days (from 14 December 2007 to 17 February 2008) with a nominal altitude of 100 km and an applied voltage of 3.1 kV. Period II includes 78.79 days (from 3 July 2008 to 15 December 2008) with 100 km and 2.5 kV. Period III includes 69.54 days (from 10 February 2009 to 28 May 2009) with 50 km and 2.5 kV. The days are in accumulation time and the dead time is about 23% for each.

KGRS consists of an actively cooled HPGe detector surrounded by a massive BGO anti-coincidence detector. The HPGe detector has a large volume (65 mm$\phi \times$ 77 mm in height). The BGO detector works to veto background neutrons from the satellite body as well as background gamma rays and charged particles. The data acquisition system contains analogue and digital boards for data processing and analyzing, and a CPU board for data handling, transmitting and command analysis. The details of the KGRS detector and its in-flight performance were reported in Kobayashi et al. in 2005 and 2013 [25,26].

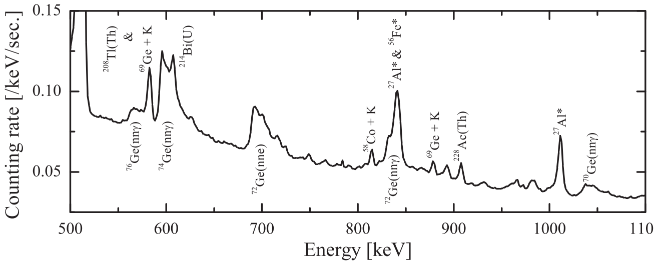

Fig. 4. Energy spectrum obtained by KGRS during Period III. Five large sawtooth peaks are included in presented energy region: $^{76}\mathrm{Ge(n, n'\gamma)}$ at 562.9 keV, $^{74}\mathrm{Ge(n, n'\gamma)}$ at 595.8 keV, $^{72}\mathrm{Ge(n, n'e)}$ at 692 keV, $^{72}\mathrm{Ge(n, n'\gamma)}$ at 834.4 keV, and $^{70}\mathrm{Ge(n, n'\gamma)}$ at 1039.3 keV.

The energy spectrum of lunar gamma rays observed in Period III is depicted in Fig. 4. Though the observed energy range is from 0.2 to 13 MeV, Fig. 4 focuses on the range of sawtooth peaks. Five sawtooth peaks with high-energy tails are clearly observed: 562.9 keV for $^{76}\mathrm{Ge(n, n'\gamma)}$ reaction, 595.8 keV for $^{74}\mathrm{Ge(n, n'\gamma)}$, 692 keV for $^{72}\mathrm{Ge(n, n'e)}$, 834.4 keV for $^{72}\mathrm{Ge(n, n'\gamma)}$, and 1039.3 keV for $^{70}\mathrm{Ge(n, n'\gamma)}$ [27]. The other ordinary peaks are made by gamma ray lines only and are generated from (n,γ) and $(n, n'\gamma)$ reactions of lunar materials, the decay series of Th and U in the Moon, and the interaction of GCRs and/or fast, epithermal and thermal neutrons with the satellite body as mainly Al and the detector itself.

In this work, peak analysis of the spectra uses the energy range of 530–780 keV including three sawtooth peaks, since 834.3 keV peak is interfered by two large peaks near the peak top such as ^{27}Al⁎ of 843.8 keV and ^{56}Fe⁎ of 846.8 keV, and 1039.3 keV peak is small. The data obtained in Periods I and III are analyzed because of different energy resolutions and the hard radiation damage in Period II. After the annealing of the HPGe crystal and the descent of the Kaguya satellite to an altitude of 30–50 km, the GRS continuously observed the lunar surface with improved energy resolution and spatial resolution, especially in Period III [26,28]. Therefore, the data of Period III is used to develop a lunar global map of LFN.

Table 1

Peak assignment for the KGRS spectrum in the energy range of 530–780 keV. C.E.@xxx keV denotes Compton edge made by a parent peak of xxx keV. Eref denotes energy of the gamma ray line given by references [10,19,27,32,33], and Efit denotes that using peak fitting in this work.

Element	Reaction	Eref	Efit	CPS	Alternates
^{212}Bi	C.E@727.3 keV	538.25	538.77	5.435E-03	
^{62}Zn+K	EC	557.30	557.58	1.420E-02	
^{76}Ge	Sawtooth	562.90	563.11	2.772E-01	
^{56}Fe	ng	569.92	570.05	2.522E−03	^{207}mPb(IT)@569.702 ^{207}Bi(EC)@569.702 ^{207}mBi(IT)@571.0 ^{56}Fe(ng)@569.92
^{74}Ge	ng	574.70	574.77	2.427E−02	^{69}Ge(EC)@574.17 ^{69}Ge(EC)+L@575.4
^{228}Ac	C.E.@772.191 keV	580.31	580.32	1.419E−02	
^{208}Tl	β(Th-Series)	583.19	583.17	2.742E−02	
^{69}Ge+K	EC	584.54	584.50	4.379E−02	^{24}Mg(ng)@585.06
^{25}Mg⁎		585.05	585.00	8.070E−02	
^{74}Ge	Sawtooth	595.80	595.64	1.192E+00	
^{73}Ge	ng	595.85	595.69	3.922E−02	^{74}Ge(nng)@595.8 ^{73}As(EC)@595.84 ^{73}As(EC)+L@597.6
^{74}As+K	EC	606.95	606.68	7.383E−03	^{74}Ge⁎@608.353 Ex. ^{73}Ge(ng), ^{74}Ge(nng)
^{214}Bi	β(U-Series)	609.31	609.01	3.953E−02	
^{43}Ca⁎		617.49	617.11	2.120E−03	
^{46}Sc⁎		627.48	627.01	2.199E−02	^{63}Ga(EC)@627.1 ^{63}Ga(EC)+L@628.12
^{63}Ga	EC	637.04	636.48	3.933E−03	63Ga(EC)+K@635.73 ^{62}Zn(Sum)(EC)@637.47 ^{62}Zn(Sum)(EC)+L@638.41 ^{198}Tl(EC)@636.4
^{72}Ge(Saw)	C.E.@834.4 keV	638.80	638.22	6.402E−03	
^{62}Zn(Sum)+K	EC	646.40	645.76	1.239E−02	^{63}Ga(EC)+K@645.67
^{56}Fe⁎	C.E.@846.6 keV	650.52	649.84	6.819E−03	
^{61}Cu	EC	656.01	655.28	3.459E−03	^{61}Cu(EC)+L@657.0
^{73}Ge	Sawtooth	658.90	658.15	3.499E−02	
^{214}Bi	U-Series	665.45	664.65	1.221E−03	^{61}Cu(EC)+K@664.341
^{63}Cu⁎	β(U-Series)	669.67	668.84	1.152E−02	^{207}mBi(IT)@669.5
^{69}Ge+K	C.E.@882.51 keV	684.37	683.43	1.779E−02	
^{72}Ge	Sawtooth	692.00	691.00	7.402E−01	
^{56}Fe	ng	692.03	691.03	2.356E−02	^{72}Ge(nng)@692 ^{201}Pb(EC)@692.37
^{70}Ge	ng	708.16	707.06	2.038E−02	^{66}Ge(EC)@705.94 ^{66}Ge(EC)+L@707.05
^{10}B⁎		718.30	717.14	3.495E−02	
^{228}Ac	β(Th-Series)	726.86	725.65	5.270E−04	
^{212}Bi	β(Th-Series)	727.33	726.11	5.593E−03	
^{73}Ge	Sawtooth	741.70	740.41	1.451E−02	
^{48}Mn	EC	752.15	750.81	2.290E−02	^{48}Mn(EC)+L@752.731 ^{30}Si(ng)@752.22 ^{204}m^{2}Bi(IT)@752.1 ^{65}Ga(EC)@751.8 ^{65}Ga(EC)+L@752.8
^{228}Ac	C.E.@968.97 keV	766.78	765.38	7.302E−03	
^{214}Bi	β(U-Series)	768.36	766.95	3.968E−03	^{65}Ga(EC)@768.2 ^{65}Ga(EC)+L@769.32
^{65}Ga+L	EC	769.32	767.91	1.251E−02	^{65}Ga(EC)@768.2 ^{65}Ga(EC)+L@769.32
^{228}Ac	β(Th-Series)	772.29	770.87	1.245E−03	
^{65}Ga+K	EC	777.34	775.90	1.245E−02	

3.2. Altitude correction

Kaguya flew at nominal altitude during each observation period. However, its actual altitude fluctuated from nominal, which was defined as the height from a spherical surface with 1737.4 km lunar mean radius. Furthermore, the lunar surface has various elevations between −9.06 km inside Antoniadi crater as the minimum and 10.75 km at southern edge of Dirichlet–Jackson basin as the maximum (a difference of 19.81 km) [29]. The solid angle or the spatial response function of KGRS viewing the Moon depends on the height of the satellite above the actual lunar surface because of the large view angle of KGRS [30]. The observed counting rate thus fluctuates due to the variation of satellite altitudes taking lunar elevation into account, even if Kaguya observes the same region. Kaguya observed the same region many times with various satellite altitudes, so the observed counting rate had to be corrected.

For variations of both flight altitude and lunar elevation, the observed count rates are normalized to an altitude of H km using a simple geometric relation between a spherical shape detector and the Moon expressed by

$$C(H) = C(h-r)\frac{\tau(H)}{\langle\tau(h-r)\rangle}, \tag{21}$$

$$\tau(x) = 1 - \sqrt{1-\left(\frac{R}{R+x}\right)^2}, \tag{22}$$

where $C(H)$ is the neutron count at an altitude of H (km) for normalization, h (km) is the altitude of the satellite, r (km) is the elevation of the Moon, R (km) is the average radius of the Moon (1737.4 km). $\tau(x)$ is the geometrical correction factor at an observation altitude of x (km), and $\langle\tau(x)\rangle$ is the average correction factor throughout the observation time. The details are presented in Appendix A.

3.3. Peak assignment and fitting condition

The peaks in the energy range of 530–780 keV are made to fit with peak functions of both Eqs. (3) and (7). In the energy region addressed here, many ordinary peaks are assigned inside and outside the sawtooth peaks as shown in Table 1. Those peaks include gamma ray lines regarded as background from the Ge crystal itself, nearby materials, the BGO scintillator, and satellite body as well as lunar gamma ray lines. These background gamma ray lines arise mainly from isomers or from electron capture (hereafter, EC) decay of radioisotopes produced inside Ge and BGO detectors by neutron activation and spallation due to GCR interaction. However, this work neglects the background lines from the BGO scintillator suggested by Weidenspointner et al. [19] because such peaks are not clearly identified in the observed spectrum. Even if they exist, they may be small due to the anti-coincidence system using BGO. In fact, there is a channel of ^{209}Bi(n, n′γ) reaction at 896.2 keV whose cross section is comparable to that of ^{70}Ge(n, n′γ) reaction at 595.8 keV [23,24], but no large peak is observed at 896.2 keV (see Fig. 4).

When ordinary peaks are on or inside the sawtooth peaks, peak fitting becomes complicated because of multi-peak fitting by two different peak functions. To reduce such complications, peak fitting for ordinary peaks should be restricted by the branching ratio or production cross section of gamma rays. In addition, when we estimate a map of LFN, the counting rate of each background peak is fixed as the average value of time variation in each period because GCR variation is very small during the observation period, especially in Period III, though background gamma ray lines are produced mainly by GCR interactions in the detectors.

Table 2
Parameters of σ as energy resolution and ρ as radiation damage.

Term	Term I	Term II	Term III
σ(keV)	2.03	2.49	2.03
ρ (keV)	1.75	0.768	1.75

Table 3
Effective ionization energy $\langle T_{Ge}\rangle$ (keV). For the 692 keV peak, $\langle T_{Ge}\rangle$ is the experimental value of 17.8 keV, not the analytical value of 11.82 keV.

Energy (keV)	Reaction	$\langle T_{Ge}\rangle$ (keV)
562.9	^{76}Ge(n, n′γ)	18.57
595.8	^{74}Ge(n, n′γ)	20.85
658.9	^{73}Ge(n, n′γ)	10.15
692	^{72}Ge(n, n′e)	11.82 (17.8)
741.7	^{73}Ge(n, n′γ)	10.93
825.6	^{73}Ge(n, n′γ)	11.70
834.4	^{72}Ge(n, n′γ)	22.37
867.8	^{73}Ge(n, n′γ)	11.27
906.7	^{73}Ge(n, n′γ)	14.06
915.8	^{73}Ge(n, n′γ)	12.73
1039.3	^{70}Ge(n, n′γ)	23.05

The parameters for peak fitting are summarized in Tables 2 and 3. The energy resolution of σ and the damage energy of ρ were determined by fitting ^{27}Al at 1014 keV peak, and the *effective* ionization energy of $\langle T_{Ge}\rangle$ is estimated as described in Section 2.3. However, the value of $\langle T_{Ge}\rangle$ for 692 keV peak is 17.80 keV as determined experimentally by sawtooth fitting, instead of 11.82 keV as estimated analytically. The similar result has been appeared in the report by Ljungvall and Nyberg, 2005 [18], which has shown that the peak of 692 keV by their experiment is broader than one by their Monte Carlo simulation.

One of the possibility of this difference may be due to neglecting background lines from the BGO scintillator. In fact, when we consider the background lines from the BGO scintillator, the spectra can be fitted with the parameter $\langle T_{Ge}\rangle$ of 11.82 eV. However, as presented in the next section, this does not become a problem for estimating LFN flux. Though σ actually depends on gamma ray energy, the difference is small in the focused energy region and has little effect on the results for sawtooth fitting.

4. Results

4.1. Sawtooth fitting

Peak functions of both Eqs. (3) and (7) with a baseline were

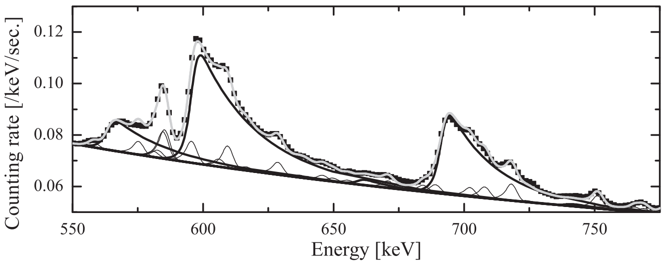

Fig. 5. Typical example of fitting results. Square: observed energy spectrum. Black thick line: fitted sawtooth peak. Thin line: fitted ordinary peak. Gray thick line: sum of all fitted peaks.

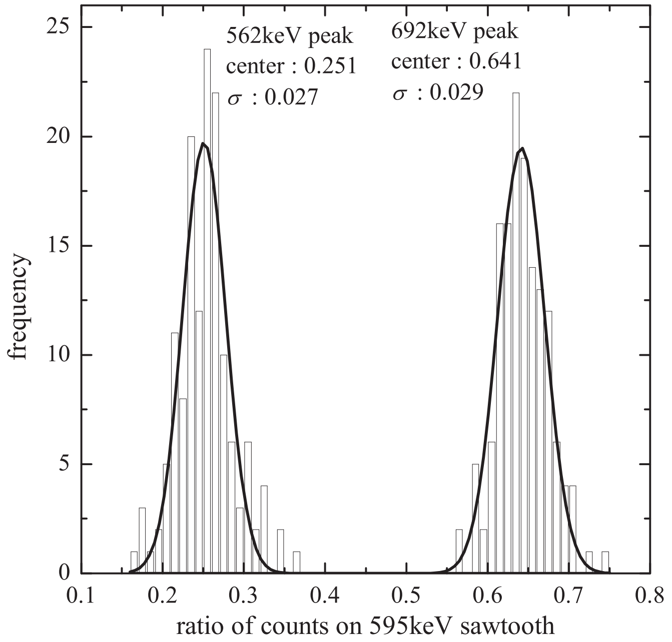

Fig. 6. Ratio of counting rates at 562 keV (left) and 692 keV (right) on the 596 keV peak. Counts are accumulated in lunar farside terrain only. “Center” is the position of the peak top.

fitted to the gamma ray spectra observed on the Moon by KGRS. An example of spectral fitting is presented in Fig. 5. In this energy region, 38 nuclides are assigned as signal candidates (see Table 1), which include three large sawtooth peaks: $^{76}\mathrm{Ge}(n, n'\gamma)$ of 562.9 keV, $^{74}\mathrm{Ge}(n, n'\gamma)$ of 595.8 keV, and $^{72}\mathrm{Ge}(n, n'e)$ of 692 keV. The counts of this spectrum were accumulated from lunar farside highland terrain that has low abundance and relatively uniformly distribution of iron and natural radioactive elements [31,30,34,35]. Therefore, since the gamma-ray peaks of such elements are small, we are able to check the results of sawtooth peak fitting without much interference of ordinary peaks. (e.g., 583.2 keV for decay of ^{208}Tl and 727.3 keV for decay of ^{212}Bi as Th-series, 609.0 keV for decay of ^{214}Bi as U-series, and 569.2 keV and 692.0 keV of $^{56}\mathrm{Fe}(n, \gamma)$, which are on/in sawtooth peaks). As clearly indicated in Fig. 5, every sawtooth peak is reconstructed well using the peak function of Eq. (7).

The histograms shown in Fig. 6 present the ratios of counting rate of each sawtooth peak to that of 596 keV sawtooth peak. The counting rates of these three peaks were derived independently without any restrictions such as interaction cross section for sawtooth peaks. Those are in good agreement with each other and the standard deviation is about 10% for 562 keV peak and about 4.5% for 692 keV peak, respectively. The former peak has larger error than the latter because of large interference peaks and a half statistics as comparing with the latter.

4.2. Temporal variation of lunar fast neutron with GCR

As LFNs are induced by interactions of GCR with lunar surface materials, temporal variations of LFNs are synchronized with those of GCRs. The daily variation of LFN during Periods I and III is plotted with that of GCR in Fig. 7, and correlation between LFN and GCR is plotted in Fig. 8. The counts of LFN were accumulated daily in lunar farside highland terrain during both periods. Iron and radioactive elements as well as other major elements such as Ca and Al are distributed relatively uniformly there compared with other lunar regions [31,30,34–36]; therefore, it can be assumed that the production rate of neutrons is relatively constant for regional variations. In Figs. 7 and 8, the counts of LFN are summed for both the 596 keV peak and the 692 keV peak. The data was already corrected for satellite altitude and lunar elevation, as explained in Section 3.2.

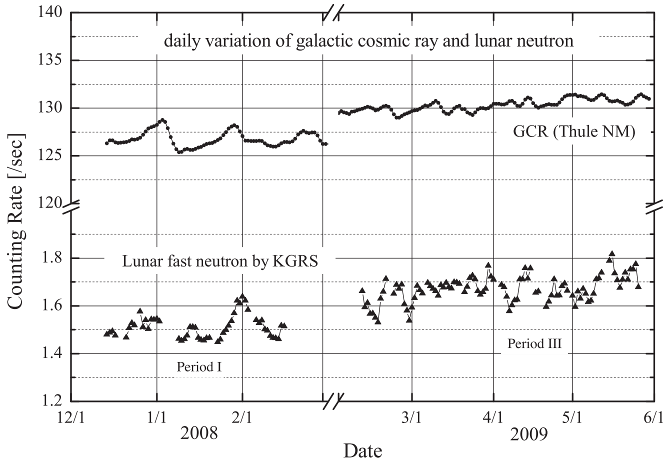

Fig. 7. Daily variation of LFNs observed by KGRS (triangles) and GRS obtained at Thule NM station (squares).

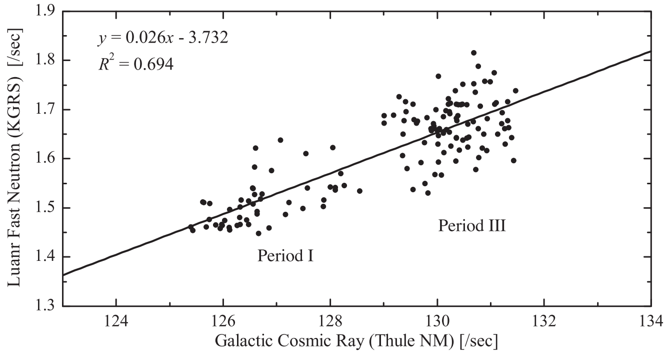

Fig. 8. Correlation of LFN and GRS. The data used are the same as in Fig. 7.

The GCR variation addressed here is based on atmospheric neutrons produced by interaction of GCR with the Earth's air atoms, which are observed by a ground-based neutron monitor at Thule station near the north magnetic pole [37]. Since the cutoff rigidity of GCR due to Earth's magnetic field is almost 0 V at Thule station, the variation of atmospheric neutrons corresponds to that of GCR in interplanetary space beyond the Earth's magnetosphere.

During the observation period, solar activity was very quiet without any large flare at the end of the 23rd solar cycle. The counting rate of GCRs increased gradually throughout the observation period. A 27-day periodic variation due to solar rotation is observed in Period I, while this periodic variation is not clear in Period III. For LNF, the counting rate also increased gradually, and the two variations seemed synchronized as shown in Fig. 7. The correlation shown in Fig. 8 has positive linearity, and the variation of LFNs (about 15%) exceeds that of GCR (about 5%). When we focus on the data of Period III only, no correlation is apparent, because the regional variation in the farside may be larger than the temporal variation introduced by GCR during the period. The Kaguya returned to the same region about every two weeks due to lunar rotation, which is about a half-period of solar rotation. Thus, a “pseudo” periodic variation may arise from the orbit of Kaguya when GCR variation is rather small. This correlation in Fig. 8 is used to correct the counting rate of LFN for GCR variation. Details are presented in Appendix B.

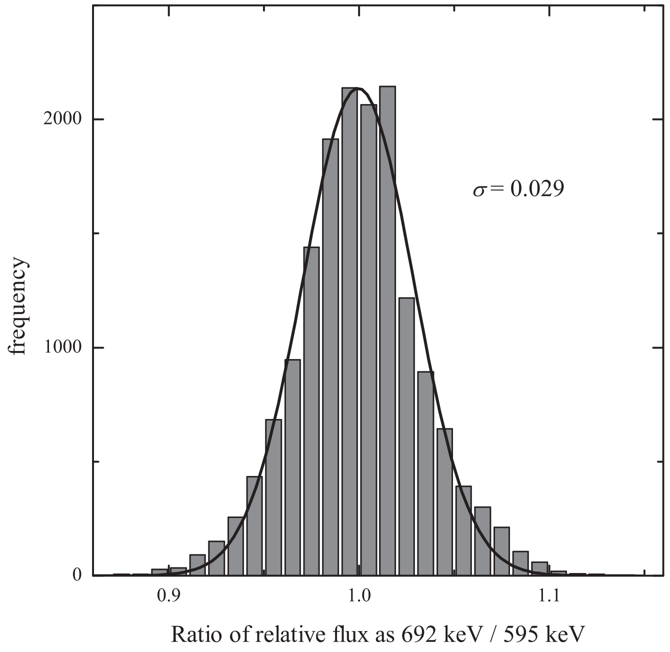

Fig. 9. Ratio of relative flux for a global map of 692 keV peak on that of 596 keV peak.

4.3. Global map of lunar fast neutron on lunar surface

To develop a lunar map of LFNs, the counts of energy spectra during Period III were divided into grids using the moving average method of a circle with radii of 150 km every 2 degrees in longitude and latitude. The gridded energy spectra were analyzed in energy ranging from 550 to 780 keV where sawtooth peaks are included at 562.9 keV, 595.8 keV, and 692 keV. The derived counting rates were normalized to the altitude of 50 km as described in Section 3.2 and corrected for GCR variation as described in Appendix B.

A histogram of the ratio of relative flux on each grid between the 595.8 keV and the 692 keV peaks is presented in Fig. 9. The magnitude of error for the sawtooth peak fitting depends on the scoped region on the Moon. Because the spacecraft was in polar orbit, the accumulation time is short in the equatorial region and long in the polar region. And the neutron flux also depends on chemical composition at local region. The errors in average (the worst case) were statistically 1.68 (2.64)% for 562.9 keV, 0.843 (1.32)% for 595.8 keV and 1.05 (1.65)% for 692 keV, and peak fitting 9.45 (18.7)% for 562.9 keV, 2.01 (3.99)% for 595.8 keV and 2.56 (5.06)% for 692 keV. These values are consistent with the histogram width of the ratio of counting rates shown in Fig. 9 and also in Fig. 6 for the lunar highland terrain. This work defines the accuracy for global map as the standard deviation of this histogram of 3%.

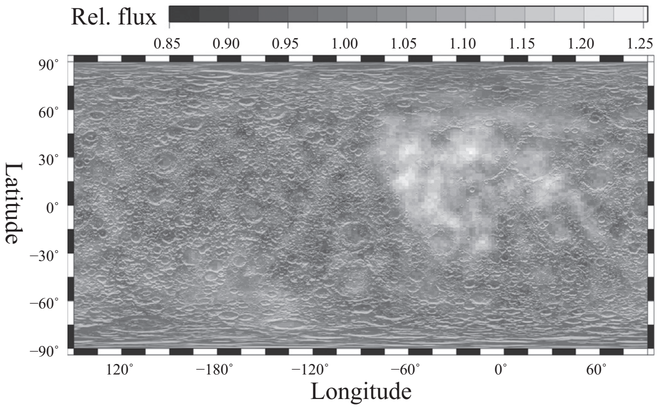

Fig. 10. Global map of LFN obtained by KGRS. The data is gridded every 2 degrees in longitude and latitude with count accumulation in a circle of 150 km radius. Rel. flux is relative flux, which is the counting rate divided by the average counting rate of the entire Moon.

The lunar map of LFN, whose counts are summed for both 595.8 keV and 692 keV peaks, except for the 562.9 keV peak with a large error due to the interference peaks, is presented in Fig. 10. The right side of the map is the nearside of the Moon facing the Earth, and the left side is the farside. The map was smoothed by a Gaussian filter with FWHM of 150 km. The nearside maria (Oceanus Procellarum, Mare Imbrium, Mare Tranquillitatis, and Mare Nubium) indicate high flux of LFN. The region west of Marius hill has the highest value, and the region south of Oceanus Procellarum and the west region of Mare Imbrium have the second-highest values. In contrast, the LFN flux is low in the farside highland. The South Pole-Aitken Basin near the South Pole on the farside has relatively high flux. These results are consistent with past observation [38].

5. Discussion

5.1. Comparison of counting rate and cross section

The ratios of counting rates in Fig. 6 reflect the ratios of cross sections for $Ge(n, n'\gamma)$ reaction because all sawtooth peaks are produced from the same neutron source of LNF and the same target of the HPGe detector. The ratio estimated analytically is 0.213 for the 562.9 keV peak and 0.186 for the 692 keV peak based on the energy spectrum of LFN [22] and the cross section of $Ge(n, n'\gamma)$ [23,24]. The abundance of Ge isotopes in the detector was assumed to be the natural abundance of Ge. The experimental ratio derived from the peak center based on Fig. 6 is 0.251 ± 0.027 for 562.9 keV peak and 0.641 ± 0.029 for 692 keV peak, respectively.

The values of 562.9 keV peak are consistent with one another, though the analytical value seems smaller than the experimental one. The counts for the 562.9 keV peak may have been overestimated by about 10%, since a large complex peak consisting of ^{208}Tl at 583.2 keV and ^{69}Ge+K at 584.5 keV is on the sawtooth peak.

For the 692 keV peak, there is a difference factor of 3.4 between the experimental value and the estimated value, due to the difference between the detection efficiency of electrons and gamma rays as explained by Lister and Smith [39]. The reaction is $^{74}Ge(n, n'\gamma)$ for 595 keV peak and $^{72}Ge(n, n'e)$ for 692 keV peak, that is, the 595 keV peak is made from emitted gamma rays with a recoil Ge atom, and the 692 keV peak is made from emitted electrons with a recoil Ge atom. In general, electrons can be detected more easily than gamma rays. The analytical ratio does not take into account detection efficiency, whereas the experimental ratio includes the effect of detection efficiency. Therefore, the experimental ratio of the 692 keV peak exceeds that of the analytical one. Past works [13,14,16,17] have reported relatively large 692 keV peaks, consistent with this work.

5.2. Comparison of the maps

A global map of LFNs was developed based on the data observed by the Neutron Spectrometer aboard Lunar Prospector (LPNS) [38]. Fig. 11 shows the relative flux map of LFN obtained by LPNS (contour lines) and the one by KGRS (gray scale) presented in Fig. 10. The LPNS data were rebinned from the original data to the

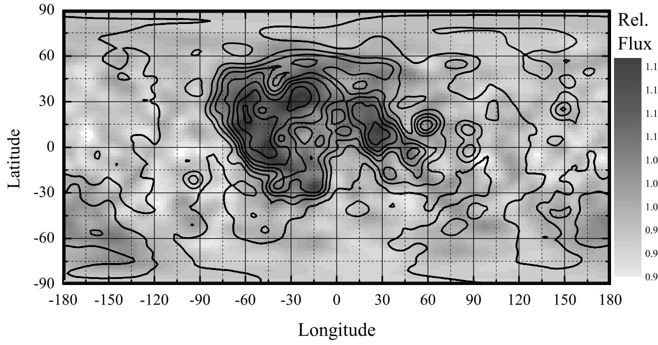

Fig. 11. Comparison of neutron maps obtained by KGRS (gray scale) and by LPNS (contour). The map of KGRS is the same as Fig. 10, and the one of LPNS was rebinned from the original data [38] to grid data, the same as in the present work.

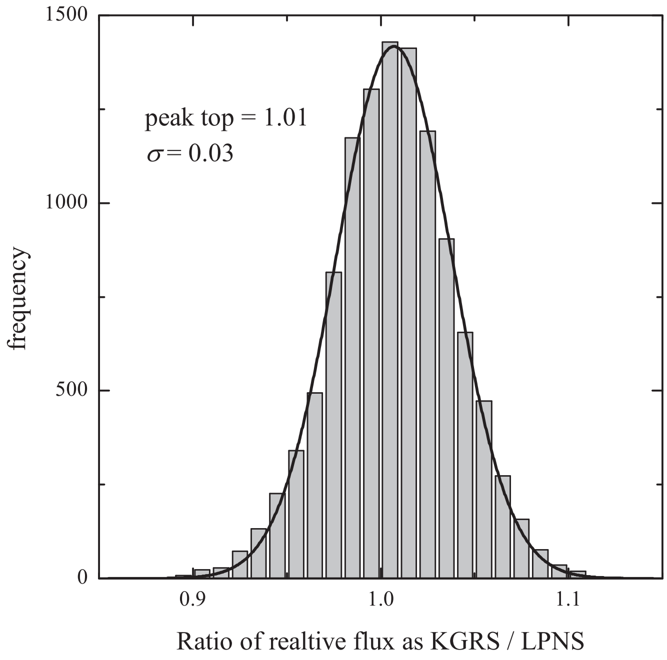

Fig. 12. Ratio of relative LFN flux of KGRS on that of LPNS. The KGRS data was rebinned to 2 × 2 degrees equal area [38].

grid data with 2-degree steps using the Gaussian filter with FWHM of 150 km as well as this work. These two maps appear to agree well with each other.

The histogram of ratio of the relative flux between LPNS and KGRS is presented in Fig. 12. The KGRS data was rebinned to 2 by 2 degrees equal area defined by LPNS [38]. The histogram has a peak top of nearly 1 and the standard deviation is 3% similar as Fig. 9. Since the standard deviation for each bin of LPNS is about 6%, the result presented here seems to be a good agreement with each other. The relative flux is the counting rate normalized by the average counting rate for the entire Moon. As a result, the detection efficiency is canceled when we calculate the relative flux. Both counting rate correction for variation of the observation height and the GCR flux is less than 1.8% and 0.23% in this work, respectively, and these corrections are smaller than the magnitude of regional variation about 20% on the Moon shown in Fig. 10. Therefore, the results presented in Fig. 12 strongly indicate that the proposed method can be used to estimate the distribution of LFNs.

6. Conclusion

This report describes a new method to estimate the relative flux of fast neutrons using a gamma ray spectrometer (GRS) consisting of an HPGe detector. Sawtooth peaks made by fast neutrons are fit with ordinary peaks made by gamma ray lines on an energy spectrum of gamma rays. A model of the sawtooth peak function takes into account the interaction of lunar fast neutron (LFNs) in the HPGe detector and the response function of the detector sustaining radiation damage. This model was applied to actual lunar gamma ray data observed by the Kaguya Gamma Ray Spectrometer (KGRS) in lunar polar orbit. The temporal variation of LFNs was found to be synchronous with that of galactic cosmic rays (GCRs) based on neutron production on the Moon. Also, the lunar map of LFN agrees well with past results obtained using the Neutron Spectrometer aboard Lunar Prospector [38]. These two facts confirm that the proposed method can estimate the relative flux of LFNs. In order to estimate absolute flux, we need simulation calculations for the spatial response function of LFNs.

In addition, the newly developed method will become an important backup for a neutron counter for planetary observations. Because gamma ray emission from nuclides on a planet is induced by interaction of neutrons there, gamma rays and neutrons must be observed simultaneously in order to correct gamma ray counts for neutron intensity. The new method will assist when a neutron detector with a GRS consisting of an HPGe detector has failed.

For gamma ray spectroscopy using a Ge detector for planets, their satellites, and asteroids, the new method is also very important for deriving their elemental distributions. Some large peaks on the sawtooth peak (e.g., ^{214}Bi of 609 keV peak of U series, ^{27}Al* of 843.8 keV and ^{56}Fe* of 846.8 keV) have not been analyzed due to the ambiguity of the sawtooth peaks. For instance, the 609 keV peak is the largest of the peaks of the decay series of uranium that is related to the thermal history of the planet. However, this method provides reliable gamma ray counts of such ordinary peaks because of highly reliable sawtooth fitting. This method allows developing highly precise lunar elemental maps even in low elemental concentration regions.

Appendix A. Correction for variation of satellite altitude and lunar elevation

The Kaguya observed a region at various altitudes from the surface. Since the field of view or solid angle of the detector for the Moon depends on height from the lunar surface, these observed counts should be corrected for height variations.

Absolute intensity of LFN at the height of x (km) from the actual lunar surface, $I(x)$, is represented as

$$I(x) = \tau(x)I(0), \tag{A.1}$$

where $\tau(h)$ is the geometrical effect of flux change during transportation from the surface to an observation height and $I(0)$ is the intensity at the surface. The altitude of Kaguya and the lunar elevation given by LALT [29] are defined as height from the spherical surface of an average lunar radius of 1737.4 km; thus, the actual height from the actual surface x becomes $x = h - r$, where h is the altitude of Kaguya and r is the lunar elevation.

When we define observation time as Δt_i and detection efficiency as ζ, counts of $N(x_i)$ observed during Δt_i at actual height x_i become

$$N(x_i) = \zeta\tau(x_i)I(0)\Delta t_i. \tag{A.2}$$

When KGRS observes a region n times (i.e., i.e. $i = 1 \sim n$), the total observed count on the region, N_{obs}, becomes

$$N_{\text{obs}} = \sum_{i=1}^{n} N(x_i) = \zeta I(0) \sum_{i=1}^{n} \tau(x_i)\Delta t_i, \tag{A.3}$$

Since total observed time T [s] becomes $T = \sum \Delta t_i$, the counting rate C_{obs} during T becomes

$$C_{\mathrm{obs}} = \frac{N_{\mathrm{obs}}}{T} = \zeta I(0)\langle\tau(x_i)\rangle, \tag{A.4}$$

where $\langle\tau(x_i)\rangle$ is the average value of $\tau(x_i)$ weighted by Δt_i represented as

$$\langle\tau(x_i)\rangle = \frac{\sum_{i=1}^{n}\tau(x_i)\Delta t_i}{\sum_{i=1}^{n}\Delta t_i}. \tag{A.5}$$

It should be noted that C_{obs}, N_{obs} and T are actual values obtained by KGRS. ζ and $\tau(x)$ are estimated by simulation calculation taking the detector setup into account. If we assume the detector has a simple shape (e.g., a board or a sphere), the geometrical effect of $\tau(x)$ can be derived analytically. Thus, the counts summed at various observed heights are translated to the absolute flux at the surface using Eq. (A.4).

For normalizing the counting rate to a nominal altitude of H, the observed counting rate can be normalized as follows because the counting rate at H is represented as $C(H) = \zeta I(0)\tau(H)$ derived from Eq. (A.2):

$$C(H) = C_{\mathrm{obs}}\frac{\tau(H)}{\langle\tau(x_i)\rangle}. \tag{A.6}$$

Thus, we consider only the geometric effect of $\tau(x_i)$ since the detection efficiency ζ is canceled out when the counting rate is normalized to an altitude.

Appendix B. Correction for time variation of galactic cosmic ray flux

We consider a time correction of neutron counts for GCR flux variation because lunar neutrons are induced by interaction of GCR with the lunar material. This work adopts atmospheric neutron counts as GCR variations that have been observed at Thule station near the Earth's north magnetic pole [37].

The counting rate of neutrons at time i, $C_n{}^i$ [/s] can be expressed as

$$C_n^i = C_n^0 + \Delta C_n^i, \tag{B.1}$$

where $C_n{}^0$ is the counting rate at a datum time and ΔC_n^i is the variation magnitude of the counting rate from $C_n{}^0$ due to GCR variation. When GCR flux does not change, the counting rate does not change between time i and datum time.

When N_{obs} expresses total observed counts of neutrons during the total observation period as T [s], N_{obs} is expanded using Eq. (B.1) as follows:

$$N_{\mathrm{obs}} = \sum_i^T C_n^i\Delta t_i = \sum_i^T \{C_n^0 + \Delta C_n^i\}\Delta t_i = C_n^0 T + \sum_i^T \Delta C_n^i\Delta t_i, \tag{B.2}$$

where Δt_i is the observation time at time i. As $C_n^0 T$ corresponds to gamma ray counts for no GCR variation, $C_n{}^0$ becomes

$$C_n^0 = \frac{N_{\mathrm{obs}}}{T} - \frac{\sum_i^T \Delta C_n^i\Delta t_i}{T} = C_{\mathrm{obs}} - \langle\Delta C_n^i\rangle, \tag{B.3}$$

where C_{obs} is the observed counting rate for total time and $\left\langle\Delta C_n^i\right\rangle$ is the average magnitude of counting rate variation. Therefore, if $\left\langle\Delta C_n^i\right\rangle$ is estimated from the observed data, we can derive the counting rate as $C_n{}^0$ normalized for GCR flux at the datum time.

$\left\langle\Delta C_n^i\right\rangle$ can be estimated as follows. Fig. 8 presented in Section 4 shows the correlation between counting rates of LFN and GCR accumulated daily in farside highland terrain, which has relatively uniform composition. Since the correlation has linearity, the slope of the line, α, becomes

$$\alpha = \frac{C_n^i - C_n^0}{C_{\mathrm{GCR}}^i - C_{\mathrm{GCR}}^0} = \frac{\Delta C_n^i}{C_{\mathrm{GCR}}^i - C_{\mathrm{GCR}}^0}. \tag{B.4}$$

Then the ΔC_n^i is estimated as

$$\Delta C_n^i = \alpha(C_{\mathrm{GCR}}^i - C_{\mathrm{GCR}}^0) \tag{B.5}$$

where C_{GCR}^i represents the atmospheric neutron count as GCR at time i and C_{GCR}^0 represents that at the datum time.

Finally, by substituting Eq. (B.5), Eq. (B.3) becomes

$$\begin{aligned} C_n^0 &= C_{\mathrm{obs}} - \frac{\sum_i^T \alpha(C_{\mathrm{GCR}}^i - C_{\mathrm{GCR}}^0)\Delta t_i}{T} \\ &= C_{\mathrm{obs}} - \frac{\alpha\left(\sum_i^T C_{\mathrm{GCR}}^i\Delta t_i - C_{\mathrm{GCR}}^0 T\right)}{T} = C_{\mathrm{obs}} - \alpha(\langle C_{\mathrm{GCR}}^i\rangle - C_{\mathrm{GCR}}^0), \end{aligned} \tag{B.6}$$

where $\left\langle C_{\mathrm{GCR}}^i\right\rangle$ is the average flux of GCR during observation period T [s]. GCR data, C_{GCR}^0 and $\left\langle C_{\mathrm{GCR}}^i\right\rangle$, were obtained from Thule station data. The slope of α is decided experimentally based on Fig. 8. Thus, the counting rate of LFN at a datum time can be derived from observed values.

Appendix C. Deriving of sawtooth function

The peak function for the sawtooth peak using Eq. (7) is derived from Eq. (1) substituting the source function Eq. (5) and the response function Eq. (6). That is,

$$P(E) = \begin{cases} \displaystyle\int_{E_\gamma}^{\infty}\frac{A}{\langle T_{\mathrm{Ge}}\rangle}\exp\left(-\frac{\varepsilon - E_\gamma}{\langle T_{\mathrm{Ge}}\rangle}\right)\frac{1}{\kappa}\frac{1}{\sqrt{2\pi}\sigma}\exp\left(\frac{\rho^2}{2\sigma^2}\right) \\ \qquad \displaystyle\exp\left(\frac{(E-\varepsilon)\rho}{\sigma^2}\right)d\varepsilon \quad (\text{if } E < E_\gamma - \rho) \\ \displaystyle\int_{E_\gamma}^{E+\rho}\frac{A}{\langle T_{\mathrm{Ge}}\rangle}\exp\left(-\frac{\varepsilon - E_\gamma}{\langle T_{\mathrm{Ge}}\rangle}\right)\frac{1}{\kappa}\frac{1}{\sqrt{2\pi}\sigma}\exp\left(-\frac{(E-\varepsilon)^2}{2\sigma^2}\right) \\ \qquad d\varepsilon \\ \qquad + \displaystyle\int_{E+\rho}^{\infty}\frac{A}{\langle T_{\mathrm{Ge}}\rangle}\exp\left(-\frac{\varepsilon - E_\gamma}{\langle T_{\mathrm{Ge}}\rangle}\right) \\ \qquad \displaystyle\frac{1}{\kappa}\frac{1}{\sqrt{2\pi}\sigma}\exp\left(\frac{(E-\varepsilon)\rho}{\sigma^2}\right) \\ \qquad \displaystyle\exp\left(\frac{\rho^2}{2\sigma^2}\right)d\varepsilon \quad (\text{if } E \ge E_\gamma - \rho) \end{cases} \tag{C.1}$$

In case of $E < E_\gamma - \rho$,

$$P(E) = \frac{A}{\sqrt{2\pi}\kappa}\frac{\sigma}{\sigma^2 + \rho\langle T_{\mathrm{Ge}}\rangle}\exp\left(-\frac{\rho^2}{2\sigma^2}\right)\exp\left(\frac{\rho(E - E_\gamma + \rho)}{\sigma^2}\right) \tag{C.2}$$

In case $E \ge E_\gamma - \rho$,

$$\begin{aligned} P(E) = {}& \frac{A}{\langle T_{\mathrm{Ge}}\rangle\kappa}\exp\left(\frac{\sigma^2}{2\langle T_{\mathrm{Ge}}\rangle^2} + \frac{\rho}{\langle T_{\mathrm{Ge}}\rangle}\right)\exp\left(-\frac{E - E_\gamma + \rho}{\langle T_{\mathrm{Ge}}\rangle}\right) \\ & \times\frac{1}{\sqrt{2\pi}\sigma}\int_{E_\gamma}^{E+\rho}\exp\left(-\frac{(\varepsilon - E + \sigma^2/\langle T_{\mathrm{Ge}}\rangle)^2}{2\sigma^2}\right)d\varepsilon \\ & + \frac{A}{\sqrt{2\pi}\kappa}\frac{\sigma}{\sigma^2 + \rho\langle T_{\mathrm{Ge}}\rangle}\exp\left(-\frac{\rho^2}{2\sigma^2}\right)\exp\left(-\frac{E - E_\gamma + \rho}{\langle T_{\mathrm{Ge}}\rangle}\right) \end{aligned} \tag{C.3}$$

Here, once ε is replaced by $y = (\varepsilon - E + \sigma^2/\langle T_{\mathrm{Ge}}\rangle)/\sigma$, the integration in Eq. (C.3) becomes

$$\frac{1}{\sqrt{2\pi}\sigma}\int_{E_\gamma}^{E+\rho}\exp\left(-\frac{\left(\varepsilon - E + \sigma^2/\langle T_{\rm Ge}\rangle\right)^2}{2\sigma^2}\right)d\varepsilon$$
$$= \frac{1}{\sqrt{2\pi}}\int_{X(E)}^{Xmax}\exp\left(\frac{y^2}{2}\right)dy, \tag{C.4}$$

where the right term is defined as $\xi(E)$ by Eq. (8) with $Xmax$ by Eq. (12) and $X(E)$ by Eq. (13). Therefore,

$$P(E) = \frac{A}{\sqrt{2\pi}\kappa}\frac{\sigma}{\sigma^2 + \rho\langle T_{\rm Ge}\rangle}\exp\left(-\frac{\rho^2}{2\sigma^2}\right)\exp\left(-\frac{E - E_\gamma + \rho}{\langle T_{\rm Ge}\rangle}\right)$$
$$\times\left\{\sqrt{2\pi}\frac{\sigma^2 + \rho\langle T_{\rm Ge}\rangle}{\sigma\langle T_{\rm Ge}\rangle}\exp\left(\frac{1}{2}\left[\frac{\sigma^2 + \rho\langle T_{\rm Ge}\rangle}{\sigma\langle T_{\rm Ge}\rangle}\right]^2\right)(\xi(E) + 1)\right\} \tag{C.5}$$

Finally, using β and λ defined in Eqs. (9) and (10), Eqs. (C.2) and (C.5) are represented by Eq. (7).

The differentiation of $P(E)$ yields

$$\frac{dP(E)}{dE} = \begin{cases} \dfrac{A\beta}{\kappa}\dfrac{\rho}{\sigma^2}\exp\left(\dfrac{\rho(E - E_\gamma + \rho)}{\sigma^2}\right) & (\text{if } E < E_\gamma - \rho) \\ \dfrac{A\beta}{\kappa}\exp\left(-\dfrac{E - E_\gamma + \rho}{\langle T_{\rm Ge}\rangle}\right)\left\{\dfrac{\lambda}{\sqrt{2\pi}\sigma}\exp\left(-\dfrac{X(E)^2}{2}\right)\right. & (\text{if } E \geq E_\gamma - \rho). \\ \left.\quad - \dfrac{\lambda\xi(E) + 1}{\langle T_{\rm Ge}\rangle}\right\} & \end{cases} \tag{C.6}$$

Since $dP(E)/dE$ becomes $A\beta\rho/\kappa\sigma^2$ in both case at $E = E_\gamma - \rho$, the sawtooth function of Eq. (7) has continuity at $E = E_\gamma - \rho$.

The maximal value (i.e., the peak top) exists at $E = E_p$, where $dP(E)/dE|_{E=E_p}$ equals 0. Since the differentiation exceeds 0 when E is less than $E_\gamma - \rho$, the peak top energy must exceed $E_\gamma - \rho$. Therefore, the peak top energy must satisfy

$$\frac{1}{\sqrt{2\pi}}\exp\left(-\frac{X(E_p)^2}{2}\right) = \frac{\sigma}{\langle T_{\rm Ge}\rangle}\left(\xi(E_p) + \frac{1}{\lambda}\right). \tag{C.7}$$

The peak top energy presented by Eq. (14) is derived from the above equation.

If a detector sustains no radiation damage, the response function of Eq. (6) becomes Gaussian only. The sawtooth function and the peak top energy then become

$$P(E) = A\exp\left(\frac{\sigma^2}{2\langle T_{\rm Ge}\rangle^2}\right)\exp\left(-\frac{E - E_\gamma}{\langle T_{\rm Ge}\rangle}\right)\xi'(E) \tag{C.8}$$

$$E_p = E_\gamma + \sigma\left(\frac{\sigma}{\langle T_{\rm Ge}\rangle} + \sqrt{2\left[\ln\left(\frac{\langle T_{\rm Ge}\rangle}{\sqrt{2\pi}\sigma}\right) - \ln(\xi'(E_p))\right]}\right) \tag{C.9}$$

where

$$\xi'(E) = \frac{1}{\sqrt{2\pi}}\int_{X(E)}^{\infty}\exp\left(-\frac{y^2}{2}\right)dy \tag{C.10}$$

These equations correspond to the case of $\rho \to \infty$ in Eq. (7) through Eq. (14). Parameter $1/\langle T_{\rm Ge}\rangle$ corresponds to parameter of b as presented in Table 3 in the paper of Siiskonen and Toivonen [17].

References

[1] D.J. Lawrence, W.C. Feldman, B.L. Barraclough, et al., Science 281 (1998) 1484–1489.

[2] W.V. Boynton, G.J. Taylor, L.G. Evans, et al., J. Geophys. Res. 112 (2007) E12S99.

[3] N. Hasebe, E. Shibamura, T. Miyachi, et al., J. Phys. Soc. Jpn. 78 (2009) 18–25.

[4] J.O. Goldsten, E.A. Rhodes, W.V. Boynton, et al., Space Sci. Rev. 131 (2007) 339–391.

[5] I.G. Mitrofanov, A. Bartels, Y.I. Bobrovnitsky, et al., Space Sci. Rev. 150 (2010) 183–207.

[6] I.G. Mitrofanov, A.B. Sanin, W.V. Boynton, et al., Science 330 (2010) 483.

[7] O. Gasnault, W.C. Feldman, S. Maurice, et al., Geophys. Res. Lett. (2001) 3797–3800.

[8] K. Alanko-Huotari, K. Mursula, I.G. Usoskin, G.A. Kovaltsov, Solar Phys. 289 (2006) 391–404.

[9] M.L. Litvaka, I.G. Mitrofanova, A.B. Sanin, et al., Planet. Space Sci. 122 (2016) 53–65.

[10] L.G. Evans, R.C. Reedy, R.D. Starr, et al., J. Geophys. Res. 111 (2006) E03S04.

[11] J. Brückner, H. Wänke, R.C. Reedy, Proc. J. Geophys. Res. (Lunar Planet. Sci. Conf. 17th) 92 (1987) E603.

[12] G.P. Škoro, I.V. Aničin, A.H. Kukoč, et al., Nucl. Instrum. Methods Phys. Res. Sect. A 316 (1992) 333–336.

[13] R. Wordel, D. Mouchel, T. Altzizoglou, et al., Nucl. Instrum. Methods Phys. Res. Sect. A 369 (1996) 557–562.

[14] G. Fehrenbacher, R. Meckbach, H.G. Paretzke, Nucl. Instrum. Methods Phys. Res. Sect. A 372 (1996) 239–245.

[15] G. Fehrenbacher, R. Meckbach, H.G. Paretzke, Nucl. Instrum. Methods Phys. Res. Sect. A 397 (1997) 391–398.

[16] E. Gete, D.F. Measday, B.A. Moftah, et al., Nucl. Instrum. Methods Phys. Res. Sect. A 388 (1997) 212–219.

[17] T. Siiskonen, H. Toivonen, Nucl. Instrum. Methods Phys. Res. Sect. A 540 (2005) 403–411.

[18] J. Ljungvall, J. Nyberg, Nucl. Instrum. Methods Phys. Res. Sect. A 546 (2005) 553–573.

[19] G. Weidenspointner, et al., Astron. Astrophys. 411 (2003) L113–L116.

[20] M. Kato, S. Sasaki, Y. Takizawa, Kaguya project, Space Sci. Rev. 154 (2010) 3–19.

[21] B. Pirard, J. Cabrera, C. d'Uston, et al., Nucl. Instrum. Methods Phys. Res. Sect. A 572 (2007) 698–707.

[22] N. Yamshita, N. Hasebe, T. Miyachi, et al., Earth Planet Space 60 (2008) 313–319.

[23] M.B. Chadwick, P. Obložinský, M. Herman, et al., Nucl. Data Sheets 107 (2006) 2931–3060.

[24] Evaluated Nuclear Data File (ENDF), National Nuclear Data Center, URL ⟨http://www.nndc.bnl.gov/exfor/endf00.jsp⟩.

[25] M. Kobayashi, N. Hasebe, H. Tsukaji, et al., Nucl. Instrum. Methods Phys. Res. Sect. A 548 (2005) 401–410.

[26] M. Kobayashi, N. Hasebe, T. Miyachi, et al., J. Instrum. 8 (2013) P04010.

[27] Evaluated Nuclear Structure Data File (ENSDF), National Nuclear Data Center, URL ⟨http://http://www.nndc.bnl.gov/ensdf/⟩.

[28] N. Yamashita, O. Gasnault, O. Forni, et al., Abstr. Eur. Planet. Sci. Congr. (2010) 580–581.

[29] H. Araki, S. Tazawa, H. Noda, et al., Science 323 (2010) 897–900.

[30] S. Kobayashi, N. Hasebe, E. Shibamura, et al., Space Sci. Rev. 154 (2010) 193–218.

[31] T.H. Prettyman, J.J. Hagerty, R.C. Elphic, et al., J. Geophys. Res. 111 (2006) E12007.

[32] L.P. Ekström, R.B. Firestone, WWW Table of Radioactive Isotopes, database version 2/28/99 from URL ⟨http://ie.lbl.gov/toi/index.htm⟩.

[33] Database for Prompt Gamma-ray Neutron Activation Analysis, International Atomic Energy Agency, URL ⟨http://http://www-nds.iaea.org/pgaa/iaeapgaa.htm⟩.

[34] N. Yamshita, N. Hasebe, R.C. Reedy, et al., Geophys. Res. Lett. 37 (2010) L10201.

[35] O. Gasnault, O. Forni, B. Diez, et al., Abstr. 40th Lunar Planet. Sci. Conf. (2009) 2253.

[36] N. Yamashita, O. Gasnault, O. Forni, et al., Earth Planet. Sci. Lett. 353–354 (2012) 93–98.

[37] Bartol Research Institute Neutron Monitor Data, The data are available from ⟨http://neutronm.bartol.udel.edu/⟩.

[38] S. Maurice, W.C. Feldman, D.J. Lawrence, et al., J. Geophys. Res. 105 (2000) E20365–E20375.

[39] D. Lister, A.B. Smith, Phys. Rev. 183 (1969) 954–963.